LANGMUIR

pubs.acs.org/Langmuir Article

Modulating the Conduction Band Energies of Si Electrode Interfaces Functionalized with Monolayers of a Bay-Substituted Perylene Bisimide

Arindam Mukhopadhyay, Kaixuan Liu, Victor Paulino, and Jean-Hubert Olivier*



Cite This: Langmuir 2022, 38, 4266-4275



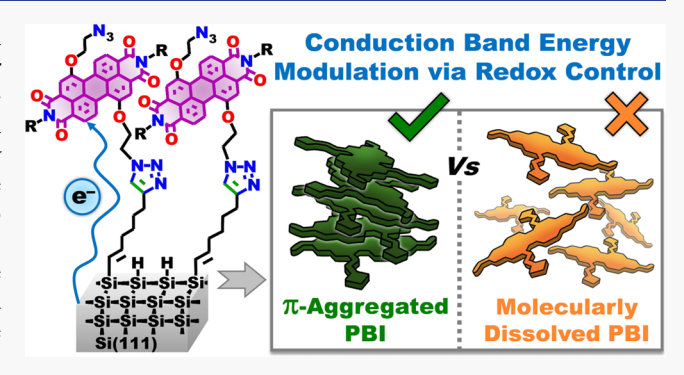
ACCESS I

Metrics & More

Article Recommendations

s Supporting Information

ABSTRACT: The confinement of π -conjugated chromophores on silicon (Si) electrode surfaces is a powerful approach to engineer electroresponsive monolayers relevant to microelectronics, electrocatalysis, and information storage and processing. While common strategies to functionalize Si interfaces exploit molecularly dissolved building blocks, only a handful number of studies have leveraged the structure—function relationships of π -aggregates to tune the electronic structures of hybrid monolayers at Si interfaces. Herein, we show that the semiconducting properties of n-type monolayers constructed on Si electrodes are intimately correlated to the initial aggregation state of π -conjugated chromophore precursors derived from bay-substituted perylene bisimide (PBI) units. Specifically, our study unravels that for n-type monolayers



engineered using PBI π -aggregates, the cathodic reduction potentials required to inject negative charge carriers into the conduction bands can be stabilized by 295 mV through reversible switching of the maximum anodic potential (MAP) that is applied during the oxidative cycles (+0.5 or +1.5 V vs Ag/AgCl). This redox-assisted stabilization effect is not observed with n-type monolayers derived from molecularly dissolved PBI cores and monolayers featuring a low surface density of the redox-active probes. These findings unequivocally point to the crucial role played by PBI π -aggregates in modulating the conduction band energies of n-type monolayers where a high MAP of +1.5 V enables the formation of electronic trap states that facilitate electron injection when sweeping back to cathodic potentials. Because the structure—function relationships of PBI π -aggregates are shown to modulate the semiconducting properties of hybrid n-type monolayers constructed at Si interfaces, our results hold promising opportunities to develop redox-switchable monolayers for engineering nonvolatile electronic memory devices.

■ INTRODUCTION

Organic-inorganic hybrid nanomaterials equipped with tunable (opto)electronic properties are ideal platforms to interrogate light-matter interaction processes, electron transfer reactions, and charge and spin transport dynamics. 1-10 "Bottom-up" molecular strategies to engineer (semi)conducting electrode surfaces functionalized with redoxresponsive molecular modules are pivotal for developing electrochemically addressable hybrid nanointerfaces. The latter has been comprehensively investigated during the past few decades to gain insights into interfacial charge-transfer processes and engineer molecular junctions, communication devices, microelectronics, actuators, field-effect transistors, nonvolatile memories, electrocatalysts, biosensors, and spin filters. 20-28 The efficiencies of such nanomaterial-based devices are primarily governed by the structure-function relationships of the hybrid interfaces that integrate the realm of organic semiconductors with that of inorganic electrodes. $^{11-28}$

Covalent functionalization of hydrogen-terminated monocrystalline silicon (Si-H) surfaces with redox-active organic

modules delivers electroresponsive nanoarchitectures. ^{14–18} Seminal studies have underscored that potentiometric attributes of Si-organic hybrid interfaces are regulated by the inherent electronic structures and the surface coverages of redox-active units that comprise anchored monolayers. ^{14–18,29–37} Synthetic design approaches and covalent functionalization strategies are equally important parameters, which have been shown to control the semiconducting properties of electro-active monolayers. ^{14–18,29–37} For example, seminal work by Fabre, Hapiot, and coworkers reported strong lateral electronic interactions between ferrocene modules anchored on Si electrodes. ³⁸ These electronic properties only emerge in functionalized Si interfaces that

Received: December 22, 2021 Revised: March 5, 2022 Published: March 30, 2022





feature a high surface coverage of ferrocene in the monolayer $(3.5 \times 10^{-10} \text{ mol cm}^{-2}).^{38}$ The confinement of redox units with the robust structural attributes of the hybrid interfaces conferred by covalent Si–C bonds is at the origin of this strong interaction. While Si-organic hybrid interfaces built from monolayers of p-type redox probes (i.e., electron donors) have been vastly explored, the repertoire of Si-organic interfaces functionalized with n-type (i.e., electron acceptor) organic building blocks is constrained only to a scant number of studies. Those However, n-type hybrid interfaces are required to engineer functional materials that find applications in solar energy capture and conversion, organic electronics, and spin filters.

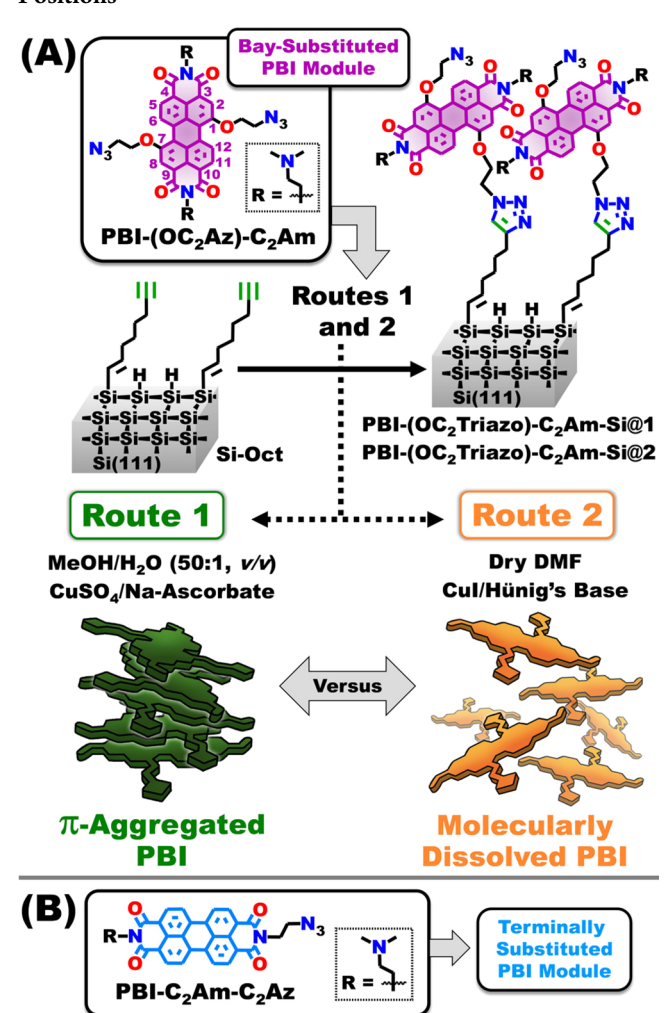
Perylene bisimide (PBI) building blocks are ideal candidates to engineer electroresponsive platforms. These redox units possess low-lying conduction band energies, electronic absorption in the visible spectral window with high oscillator strength, and chemical robustness over a broad range of temperature and pH. $^{46-50}$ In addition, their well-established assembly properties deliver π -conjugated superstructures relevant to solar energy capture and conversion and charge transport. $^{46-50}$ Noncovalent interactions between PBI units lead to long- and short-range electronic couplings, which regulate the optical and potentiometric properties of the emergent superstructures. $^{51-57}$ As shown by Spano, structural perturbations as small as Ångstrom-level displacements dramatically impact these electronic couplings, thereby altering the photophysical and potentiometric properties of PBI-derived supramolecular constructs. 58,59

Functionalizing PBI cores at the "bay regions", namely, positions 1, 6, 7, and 12 in Scheme 1, enables tuning of their electronic structures and offers a synthetic handle to monitor the formation of supramolecular architectures. ^{46–50} It is well documented that installing substituents at the "bay regions" of the PBI core contorts the π -conjugated framework that adopts a twisted conformation. ^{46–50,53,60} Consequently, the extent of frontier molecular orbital overlaps and supramolecular assembly properties differs divergently from those evidenced with analogous superstructures derived from terminally substituted PBIs where the bay regions are flanked with hydrogen atoms. ^{46–50,53,60}

In one of our recent investigations, we developed hybrid Si interfaces that feature *n*-type monolayers formed by anchoring π -aggregates of the terminally substituted PBI module PBI-C₂Am-C₂Az shown in Scheme 1B.³⁷ We showed that the conduction band energy of this class of n-type Si interfaces is intimately related to the maximum anodic potential (MAP) reached during the anodic sweep. Precisely, the first reduction potential of the PBI monolayer is stabilized by more than 375 mV at MAP = +1.5 V compared with that monitored when an MAP = +0.5 V is used.³⁷ Spurred by these results, we aimed to interrogate the scope of this redox-assisted stabilization effect by altering the structural features of PBI precursor building blocks. Because the assembly properties of bay-substituted PBIs are known to differ from those of analogous terminally substituted PBIs, we questioned if the structure-function relationships of their π -aggregates would lead to the formation of monolayers whose conduction band energies can be dynamically switched as a function of MAPs.

In this present study, we establish the covalent modification of alkyne-terminated monolayers on Si electrodes with the novel bay-substituted PBI unit $PBI-(OC_2Az)-C_2Am$ shown in Scheme 1A. The PBI-functionalized n-type monolayers at Si

Scheme 1. (A) Access to PBI-Functionalized Monolayers (PBI-Sis) Engineered on Hybrid Si Electrode Interfaces via Cu⁺¹-Catalyzed "Click" Reactions of the Alkyne-Terminated Si-Oct Precursor Interface with the Bay-Substituted PBI Module PBI-(OC₂Az)-C₂Am.^a (B) Molecular Structure of the Terminally Substituted PBI Module PBI-C₂Am-C₂Az that Features an Azide Substitution at one of the Two Imide Positions



"Note that routes 1 and 2 offer synthetic leverage to control the aggregation state of PBI-(OC₂Az)-C₂Am during the construction of monolayers on the Si-Oct precursor interface.

interfaces (PBI-Sis) created in this manner exhibit conduction band energies that can be modulated electrochemically. We demonstrate that the cathodic reduction potentials required to inject negative charge carriers into the conduction bands of such n-type monolayers are intimately associated with the maximum anodic potential (MAP) used during the anodic oxidation cycles. Specifically, the PBI monolayer built from PBI-(OC₂Az)-C₂Am π-aggregates unveils a first cathodic reduction potential at -0.455 V vs Ag/AgCl when using a low MAP of +0.5 V. In contrast, the conduction band energy undergoes significant stabilization by 295 mV under the influence of a high MAP of +1.5 V. This energetic stabilization is fully reversible and can be switched by changing the MAP between the limits of +0.5 and +1.5 V. A set of control experiments confirm that such redox-assisted conduction band stabilization is absent for (1) analogous n-type monolayers

engineered from molecularly dissolved PBI chromophores and (2) Si interfaces that are characterized with a low surface coverage of PBI units. Our findings are rationalized based on non-negligible conformational perturbations of the π -aggregated PBI monolayer upon p-doping, which occurs at a high MAP of +1.5 V. The latter engenders electronic trap states that enable electron injection into the conduction band at much lower cathodic potentials.

■ EXPERIMENTAL SECTION

Synthesis of PBI-(OC₂Triazo)-C₂Am-Si@1/2 Interfaces. These two PBI-Si interfaces were accessed via Cu⁺¹-catalyzed alkyne-azide "click" reaction of Si-Oct with PBI-(OC2Az)-C2Am via routes 1 and 2 shown in Figure S8. In a typical procedure, Si-Oct interface was immersed in an Ar-degassed solution of PBI-(OC2Az)-C2Am (concentration = 0.7 mM; total volume of the reaction = 50 mL, solvent = MeOH or DMF). Subsequently, solutions of the Cu⁺¹ catalysts (i.e., anhyd CuSO₄/Na-ascorbate or anhyd CuI/Hünig's base) were prepared in the pertinent degassed solvents (i.e., H2O or DMF) under Ar. It should be noted that in each case, the Cu-salt (i.e., CuSO₄ or CuI) was used in 10 mol % with respect to the amount of PBI precursors. However, Na-ascorbate or Hünig's base was used in 10 molar equivalents with respect to the amount of the Cu-salt, and, thus, 1 molar equivalent with respect to the amount of PBI. Accordingly, in each case, the Cu⁺¹ catalyst solution was cannulated dropwise (under Ar) into the reaction mixture contained in the flask and the contents were allowed to stir gently under Ar at rt for 1 d. After this period, the solution of the reaction mixture was removed, and the resultant PBI-(OC2Triazo)-C2Am-Si@1/2 surface was subjected to comprehensive sequential washing with copious amounts of water, DMF, MeOH, DCM, respectively, and finally with water. Subsequently, the PBI-Si surface was rinsed thoroughly with EDTA solution (0.05% w/v in water) to remove residual trace amounts of Cu salts adhered onto the surface. After this, the surface was washed with abundant amounts of water to preclude traces of EDTA. After these post-synthetic work-up steps, the PBI-Si surface was dried briefly by a gentle stream of Ar followed by high vacuum conditions via standard Schlenk procedures.

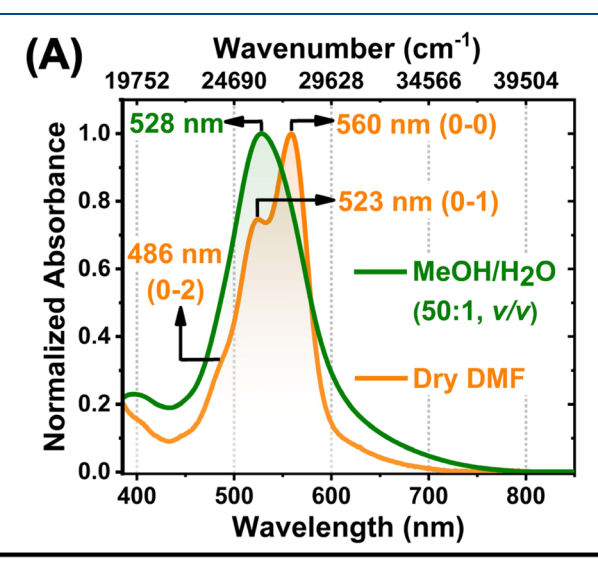
Synthesis of PBI-(OC₂Triazo)-C₂Am-Si(1:50)@1 Interface. The 'surface diluted' interface Si-(1:50)-Oct was accessed from Si-H precursor using the thermally activated grafting approach with mixed alkynes (namely, 1,7-octadiyne and 1-octyne) as shown in our previous studies. ^{36,37} Please note that the surface coverage of reactive alkyne functionalities in Si-(1:50)-Oct (~1 moiety per 20 nm²) is ca. 50 times lower compared with that evidenced in Si-Oct. ^{36,37} Accordingly, the PBI-(OC₂Triazo)-C₂Am-Si(1:50)@1 interface shown in Figure S9 was accessed from Si-(1:50)-Oct via Cu⁺¹-catalyzed "click" reaction with PBI-(OC₂Az)-C₂Am following the route 1 exactly as described earlier for analogous PBI-(OC₂Triazo)-C₂Am-Si@1 interface, cf. Tables S1 and S2. The target PBI-(OC₂Triazo)-C₂Am-Si(1:50)@1 interface was obtained by following the same post-synthetic work-up and drying process mentioned earlier.

Detailed synthetic procedures and characterization data for the PBI precursors are described in Section 2 of the Supporting Information. Solution-phase electrochemistry, AFM, SEM, and XPS characterization, and control experiments ruling out the oxidation of the Si surfaces are also detailed in the Supporting Information.

RESULTS AND DISCUSSION

Synthesis and Aggregation Properties of PBI Precursors. The novel PBI-based building block PBI- (OC_2Az) - C_2Am shown in Scheme 1A is substituted at the 1,7-bay positions with 2-azidoethoxy moiety. It has been designed to exist in the form of π -aggregates or molecularly dissolved units as a function of the solvation environment. The synthetic pathway to access this azide-functionalized bay-

substituted PBI building block uses a nucleophilic aromatic substitution reaction (SNAr) of the bromo-functionalized PBI precursor PBI-(Br)- C_2Am with 2-azidoethanol. Section 2 of the Supporting Information details synthetic procedures and characterization data. The lack of hydrophilic functionalities (e.g., cationic/anionic side chains) on the PBI-(OC_2Az)- C_2Am scaffold decreases its solubility in polar protic solvents enabling the formation of π -aggregates in this environment. In contrast, a polar aprotic medium (DMF) supports the solvation of PBI-(OC_2Az)- C_2Am as molecularly dissolved species. Figure 1A chronicles the ground-state electronic



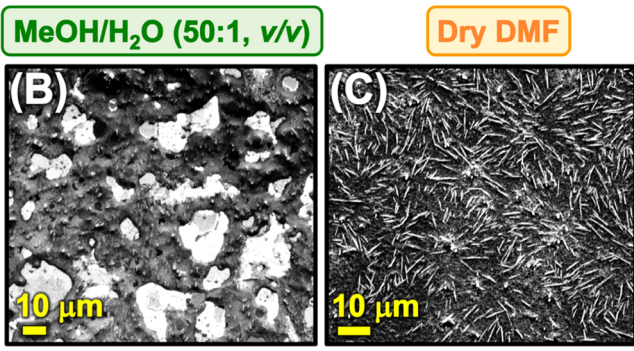


Figure 1. (A) Normalized ground-state electronic absorption spectra (GS-EAS) recorded for the solutions of PBI-(OC₂Az)-C₂Am in MeOH/H₂O (50:1, v/v) and dry DMF that is represented in green and orange lines, respectively. Experimental conditions: [PBI] = 0.7 mM; optical pathlength = 2 mm; temperature = 25 °C. (B,C) SEM images that reveal the solid-state morphologies of PBI-(OC₂Az)-C₂Am recorded for the samples prepared by drop-casting the PBI solutions (0.7 mM) in (B) MeOH/H₂O (50:1, v/v) and (C) dry DMF onto untreated Si/SiO_x substrates.

absorption spectra (GS-EAS) recorded for the solutions of PBI-(OC₂Az)-C₂Am in MeOH/H₂O (50:1 v/v) and DMF. The PBI building block exhibits the spectroscopic signatures of molecularly dissolved species in DMF (orange line in Figure 1A) as validated by (1) the 0–0, 0–1, and 0–2 vibronic transitions centered at 560, 523, and 486 nm, respectively, that are regularly separated by ~169 meV, i.e., ~1360 cm⁻¹ (the stretching frequency C=C) and (2) the relative ratio of absorbances of the 0–0 and 0–1 vibronic transitions (1.35) that indicate the absence of inter-chromophore interactions (short- and long-range coupling) between the PBI

units. 37,48,53,54,56-59 The spectroscopic signatures evidenced for the solution of PBI-(OC2Az)-C2Am building block in MeOH/H₂O (50:1 v/v) diverge from those observed in the case of the solution in DMF. Specifically, the absorption spectrum shown as a green line in Figure 1A reveals a broadband feature with an absorption maximum at 528 nm and diagnoses unresolved vibronic transitions. These spectroscopic features suggest the existence of π -aggregated species in MeOH/H₂O (50:1, v/v) that exhibit non-negligible excitonic coupling between the PBI units. 37,48,53,54,56-59 The hypsochromic shift (1082 cm⁻¹) calculated when comparing the spectroscopic signatures of PBI-(OC2Az)-C2Am building blocks in MeOH/H₂O (λ_{max} = 528 nm) and DMF (λ_{max} = 560 nm) suggests that H-like aggregates are the primary species. In addition, the tail observed between 600 and 700 nm may also indicate the existence of J-like aggregate although at a smaller concentration.

Interrogated by scanning electron microscopy, the solidstate morphologies of the PBI-(OC2Az)-C2Am blocks dropcast from parent DMF and MeOH/H2O solutions are different. As shown in Figures 1B and S5, drop-casting a solution of PBI-(OC₂Az)-C₂Am from MeOH/H₂O (50:1, v/ v) initiates the formation of film-like materials that stem from the interaction of the solvated PBI-(OC₂Az)-C₂Am π aggregates. Please refer to Section 3 of the Supporting Information for more details on the sample preparation and data acquisition. In contrast, the SEM images in Figures 1C and S6 (drop-cast DMF solution) reveal the existence of isolated rod-like microstructures with lengths ranging between 4 and 6 µm. These well-defined hierarchical microstructures originate from the assembly of molecularly dissolved PBI units during the drop-casting process. The disparity observed when comparing the solid-state morphologies recorded for the DMF and MeOH/H₂O samples confirms that the PBI-(OC₂Az)-C₂Am building blocks exist under different solvated states.

Potentiometric Properties of Solvated PBI Precursors. The potentiometric properties recorded for the PBI-(OC2Az)-C2Am building block in DMF and MeOH/H2O confirm the existence of aggregated states. These π -aggregates do not share the same electronic structure as the molecularly dissolved building blocks. The cyclic voltammograms recorded for the molecularly dissolved species PBI-(OC2Az)-C2Am in DMF (Figures 2B and S7B) exhibit typical electrochemical reversibility⁶¹ as validated by (1) two sequential cathodic signals pertinent to the first and second reduction of a neutral PBI unit and corresponding two sequential anodic signals pertinent to the back-oxidation of the di- and monoanionic PBI species, 37,48,62,63 (2) a peak-to-peak separation ($\Delta E^{(p)}$) of 70 mV between the cathodic and anodic peaks, and (3) the ratio of the cathodic and anodic peak currents being close to unity. In contrast, the CVs recorded for the PBI-(OC₂Az)- C_2 Am π -aggregates formed in MeOH/H₂O (50:1, v/v) (Figures 2A and S7A) unambiguously underscore nonreversible 61 electrochemical processes as corroborated by (1) emergence of only one broad and unresolved cathodic reduction wave and the corresponding anodic oxidation wave, (2) a sizable peak-to-peak separation ($\Delta E^{(p)} = 125$ mV) between the cathodic and anodic peaks, and (3) deviation of the ratio of the cathodic and anodic peak currents from unity (>1). The origin of such deviation from electrochemical reversibility is traced back to slower rates of electron transfer processes and structural reorganization within the π -aggregates upon cathodic reduction and anodic back-oxidation. A similar

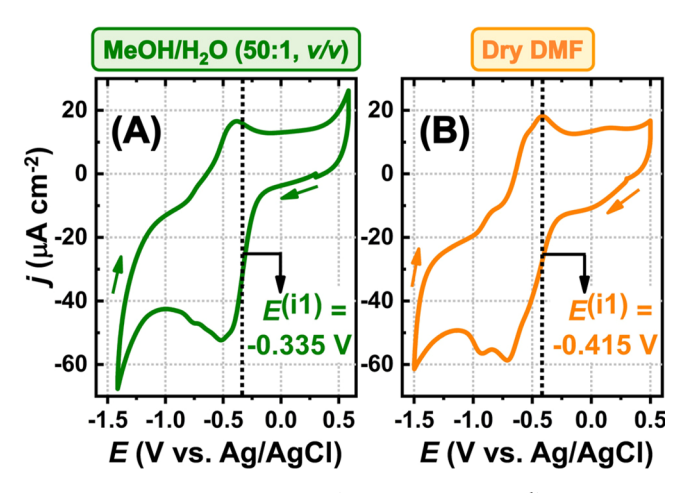


Figure 2. Cyclic voltammograms (scan rate = 0.05 Vs^{-1}) recorded for the degassed solutions of **PBI-(OC₂Az)-C₂Am** in (A) MeOH/H₂O (50:1, v/v) and (B) dry DMF using n-Bu₄NPF₆ (0.1 mM) as the supporting electrolyte. Please notice the values of the first inflection reduction potential,that is, $E^{(i1)}$, as determined from the first derivative plots of the cathodic signals in the two cases. Experimental conditions: [PBI] = 0.7 mM; working electrode = glassy carbon (electro-active surface area = 0.071 cm^2); reference electrode = Ag/AgCl (3 M NaCl); counter electrode = Pt; Ar gas atmosphere; temperature = $25 \, ^{\circ}$ C.

observation has recently been reported for related molecular systems. 36,37,64-66 Further insights into the potentiometric properties of the PBI-(OC₂Az)- C₂Am π-aggregates were gathered through estimation of the first cathodic reduction inflection potential $(E^{(i1)})$ by plotting the first derivative of the cathodic signal of the CV.67 This approach established by Vulley and coworkers estimates the half-wave potential $(E^{(1/2)})$ for nonreversible electrochemical systems.⁶⁷ As depicted in Figures 2 and S7, the PBI- (OC_2Az) - C_2Am π -aggregates formed in MeOH/H2O (50:1, v/v) feature a first reduction inflection potential $(E^{(i1)} = -0.335 \text{ V})$ that is stabilized by more than 80 mV compared to that recorded for the molecularly dissolved PBI- (OC_2Az) - C_2Am units $(E^{(i1)} =$ -0.415 V) in DMF. This observed stabilization originates from a non-negligible degree of electronic perturbation via inter-chromophore interactions within the PBI π -aggregates. 37,48,51-59 This conclusion is corroborated by the results obtained from the GS-EAS properties of the π -aggregates that reveal excitonic coupling between the π -conjugated PBI units.

Functionalization of Si Electrodes with PBI π -Aggregates. The aggregated state of PBI-(OC₂Az)-C₂Am building blocks is leveraged to construct hybrid semiconducting interfaces on Si electrodes. As shown in Scheme 1A, the Cu⁺¹-catalyzed "click" reaction in route 1 anchors the PBI- (OC_2Az) - C_2Am π -aggregates on the Si-Oct interface precursor leading to PBI-(OC2Triazo)-C2Am-Si@1 hybrid interface. The analogous Si hybrid interface PBI-(OC₂Triazo)-C2Am-Si@2 is engineered from the covalent grafting of molecularly dissolved PBI-(OC₂Az)-C₂Am units in route 2. The latter serves as a control platform to elucidate the influence of π -aggregated states on the final potentiometric properties of the Si hybrid interfaces. The synthetic procedures for these PBI-Si hybrid interfaces are described in Section 5A of the Supporting Information. Tapping mode atomic force microscopy (AFM) reveals the solid-state morphologies featured by these two analogous PBI-Si interfaces. The representative AFM images recorded for the PBI-

(OC₂Triazo)-C₂Am-Si@1 and PBI-(OC₂Triazo)-C₂Am-Si@2 interfaces are depicted in Figures 3A and S10, respectively.

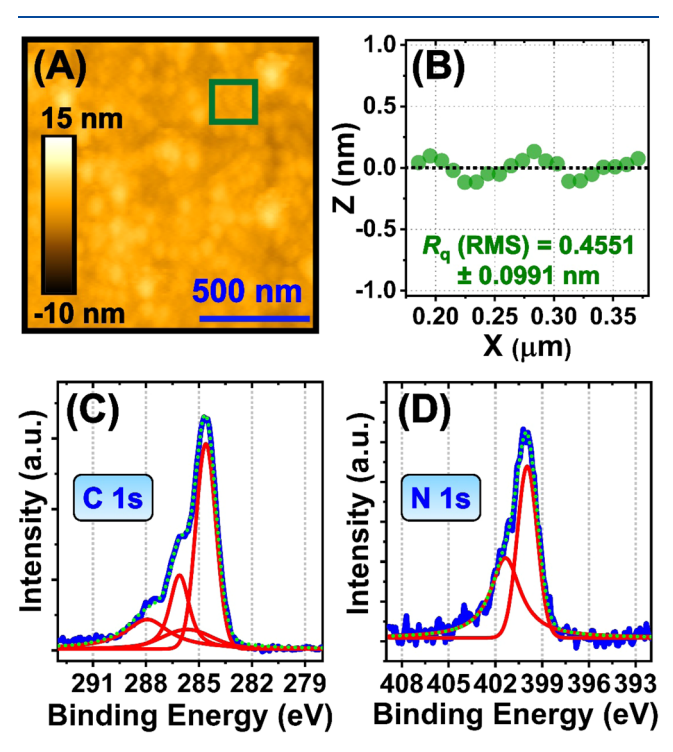


Figure 3. (A) AFM topographic image (tapping mode) of the PBI- $(OC_2Triazo)$ - C_2Am -Si@1 interface. (B) Determination of R_a (RMS) surface roughness from the cross-section profile (designated in green filled circles) of the representative area shown within the inset of the AFM image (designated in green square). (C,D) High-resolution XPS spectra (blue), deconvoluted spectra using Voigt functions (red), and cumulative fitted spectra (dotted green) evidenced for PBI-(OC₂Triazo)-C₂Am-Si@1 interface that represents the emission signals originating from (C) C 1s and(D) N 1s areas. Please note that the C 1s emission signal(C) can be deconvoluted into four Voigt functions with their peaks centered at the binding energies of 287.9, 286.1, 285.7, and 284.6 eV, which can be attributed to the contributions from \underline{C} =O, \underline{C} -O, \underline{C} -N, and \underline{C} = $\underline{C}/\underline{C}$ - \underline{C} bonds, respectively. The N 1s signal(D) can be deconvoluted into two Voigt functions with their peaks centered at the binding energies of 401.4 and 400.0 eV, validating the presence of chemically disparate nitrogen atoms.

Smooth and atomically flat surfaces are observed for both hybrid monolayers as confirmed by the root mean square surface roughness parameter, $^{30,35-37}$ $R_{\rm q}$ (RMS), which falls below 0.5 nm for the two surfaces (Figures 3B and S10). This surface morphology analysis via AFM suggests that the covalent grafting strategies using π -aggregated and molecularly dissolved states of PBI-(OC₂Az)-C₂Am deliver smooth PBI-Si hybrid interfaces that are uniformly functionalized.

To unambiguously confirm the covalent functionalization of the PBI units at the Si interface, chemical compositions of the two **PBI-Si** interfaces were examined using X-ray photoelectron spectroscopy (XPS). Please refer to Section 7 of the Supporting Information for details. The high-resolution XPS spectra of the C 1s and N 1s areas recorded for the **PBI-(OC₂Triazo)-C₂Am-Si@1** surface are shown in Figure 3C,D, respectively. Accordingly, the C 1s emission signal can be deconvoluted into four Voigt functions with their peaks centered at the binding energies of 287.9, 286.1, 285.7, and 284.6 eV. The high-energy emission peak at 287.9 eV is

diagnostic of oxygen-bonded carbon atoms (\underline{C} =O), while the emission signals peaking at 286.1, 285.7, and 284.6 eV are attributed to oxygen-bonded carbon (C-O), nitrogen-bonded carbon (\underline{C} -N), and carbon-bonded carbon (\underline{C} - C/\underline{C} =C) atoms, respectively. Notably, the emission peak at the binding energy of ~286 eV stemming from C-O bonds may also originate from contamination of external carbon sources. 36,37 The high-resolution XPS spectrum of the N 1s area (Figure 3D) offers a more explicit spectroscopic handle to unambiguously validate the covalent anchorage of the PBI units on the Si-Oct precursor interface. The N 1s emission signal can be deconvoluted into two Voigt functions with their peaks centered at 401.4 and 400.0 eV. These spectroscopic signatures confirm the presence of chemically dissimilar nitrogen atoms. Furthermore, brief scrutiny of the highresolution XPS spectrum of the Si 2p area (Figure S12) discloses the existence of SiO_x species, albeit in negligible quantities, as corroborated by the weak-intensity emission signal centered at the binding energy of 102.5 eV that implies a low level of oxidation of the precursor Si-H surface. Taken together, the XPS analyses of PBI-(OC₂Triazo)-C₂Am-Si@1 surface confirm covalent grafting of PBI units at the Si interface. The high-resolution XPS characterization data of the analogous PBI-(OC2Triazo)-C2Am-Si@2 surface are presented in Figure S13. They also confirm the successful anchorage of the *n*-type redox probe at the Si interface.

Potentiometric Properties of PBI Monolayers on Si Electrodes. The semiconducting properties of the PBI-Si hybrid interfaces are intimately related to the aggregated state of the PBI-(OC2Az)-C2Am precursors used in routes 1 and 2. As seen in Figures 4A and S18, the CVs recorded with the PBI-(OC₂Triazo)-C₂Am-Si@1 interface derived from PBI πaggregates show broad, ill-resolved, and weakly defined redox waves. This nonreversible electrochemical behavior stems from (1) slow rates of electron transfer processes and (2) structural reorganizations of the monolayer level. 36,37,64,68 Noteworthy, the CVs are reproducible, indicating that the experimental conditions used are nondestructive to the monolayer at the interface. Figures 4A, S18, and S19 reveals that the initial first reduction inflection potential $(E^{(i1)}_{Cycle 1} = -0.390 \text{ V})$ undergoes a modest cathodic shift during cycle 2 $(E^{(i1)}_{Cycle\ 2})$ = -0.455 V) and cycle 3 ($E^{(i1)}_{Cycle\ 3} = -0.460$ V). This shift may suggest that the PBI monolayers experience conformational changes, to some extent, during the cathodic sweep in cycle 1.37 Contrasting this finding, increasing the MAP to +1.5 V has a remarkable influence on the cathodic reduction waves. Specifically, Figures 4B, S20, and S21 shows that the first reduction inflection potential recorded in cycle 2 $(E^{(i1)}_{Cycle\ 2} =$ -0.160 V) is stabilized by 295 mV compared with that evidenced in cycle 2 when applying a MAP = +0.5 V $(E^{(i1)}_{\text{Cycle 2}})_{\text{Cycle 1}} = -0.455 \text{ V}$). It is interesting to note that (1) the $E^{(i1)}_{\text{Cycle 1}}$ recorded for the first cathodic signal remains unaltered for both MAP = +0.5 V and MAP = +1.5 V; (2) the energetic stabilization of the first reduction inflection potential is absent for MAP = +0.5 V and is only operational when a MAP = +1.5 V is reached; and (3) the energetic stabilization of $E^{(i1)}_{\text{Cycle 2}}$ remains similar upon an additional redox cycle, that is, cycle 3, with a MAP of +1.5 V ($E^{(i1)}_{\text{Cycle 3}}$ = -0.230 V).

The stabilization of the conduction band energy triggered at high MAP as chronicled in Figures 5A, S29, and S30, the $E^{(i1)}$ recorded for PBI-(OC₂Triazo)-C₂Am-Si@1 interface upon applying a MAP = +1.5 V ($E^{(i1)}$ _{Cycle 2}) can be switched back to

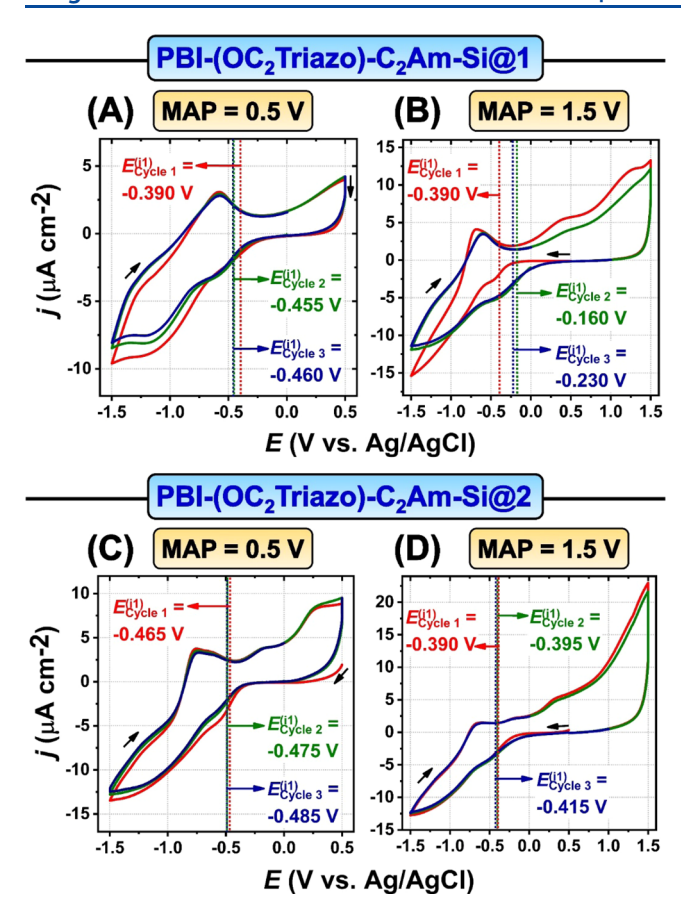


Figure 4. Cyclic voltammograms (cycles 1–3; scan rate = 0.05 Vs⁻¹) of **PBI-(OC₂Triazo)-C₂Am-Si@1** (A,B) and **PBI-(OC₂Triazo)-C₂Am-Si@2** (C,D) interfaces recorded by using a starting potential of +0.5 V in cycle 1 and the maximum anodic potential (MAP) limit of +0.5 V (A,C) and +1.5 V (B,D) during cycle 2/3 in dry acetonitrile using n-Bu₄NPF₆ (0.1 M) as the supporting electrolyte. Experimental conditions: working electrodes = **PBI-Si** surfaces (electro-active surface area = 0.5026 cm²); reference electrode = Ag/AgCl (3 M NaCl); counter electrode = Pt; Ar gas atmosphere; temperature = 25 °C. Please note that (i) the starting potential in cycle 1 for all the cases is +0.5 V, (ii) cycles 1, 2, and 3 are represented in red, green, and blue lines, respectively, and (iii) the values of $E^{(i1)}$, that is, the first inflection reduction potential as determined from the first derivative plots of the cathodic signals, are shown for the three consecutive cycles.

the original value $(E^{(i1)}_{\text{Cycle 1}})$ by resetting the MAP to +0.5 V (i.e., $E^{(i1)}_{\text{Cycle 3}})$. A similar redox-assisted stabilization effect has been recently reported by us although for monolayers constructed using terminally substituted PBI units that feature hydrogens at the 1,7 positions.³⁷ Furthermore, the reported effect is unlikely to originate from oxidation of the Si surface during the anodic sweep. While an identical MAP = 1.5 V is used when probing the potentiometric of PBI-(OC₂Triazo)-C₂Am-Si@1/2 interfaces, only the interface derived from PBI π -aggregates exhibits a stabilized conduction band energy. Should this effect stem from Si oxidation, both interfaces would demonstrate it.

No redox-assisted stabilization effect is evidenced for the PBI-(OC₂Triazo)-C₂Am-Si@2 interface constructed with molecularly dissolved PBI units (route 2 in Scheme 1A). As gleaned in the CVs recorded for the PBI-(OC₂Triazo)-C₂Am-Si@2 interface (Figures 4C,D and S22-S25), the MAP used during the anodic sweeps at +0.5 and +1.5 V has virtually no

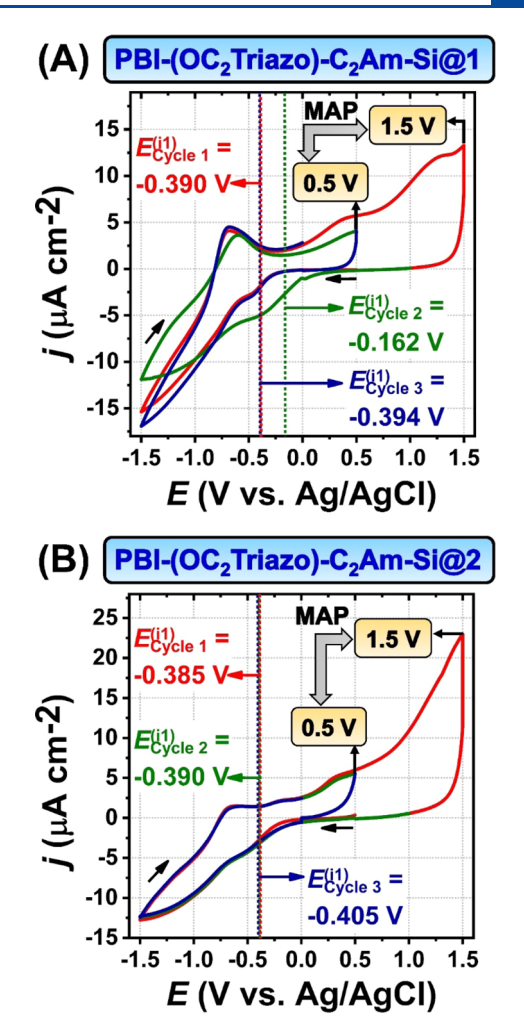


Figure 5. Sequential MAP-dependent cyclic voltammograms (cycles 1–3; scan rate = $0.05~\rm Vs^{-1}$) of PBI-(OC₂Triazo)-C₂Am-Si@1 (A) and PBI-(OC₂Triazo)-C₂Am-Si@2 (B) interfaces that employ a starting potential of +0.5 V in cycle 1 (red line) and sequentially exploit a MAP limit of +1.5 and +0.5 V during cycle 2 (green line) and cycle 3 (blue line), respectively. Please note that in the case of PBI-(OC₂Triazo)-C₂Am-Si@1, the $E^{(i1)}$ recorded during cycle 2 can be reversibly restored to its original value (that is observed in cycle 1) by resetting the MAP from +1.5 (cycle 2) to +0.5 V (cycle 3). In the case of PBI-(OC₂Triazo)-C₂Am-Si@2, however, the $E^{(i1)}$ exhibits inconsequential dependence on the MAP limit, that is, +0.5 or +1.5 V, during different cycles.

impact on the reduction inflection potentials. Precisely, exploiting a MAP of +0.5 V is associated with $E^{(i1)}_{Cycle\ 1}=-0.465$ V, which remains identical during subsequent sweeps, that is, cycles 2 and 3 in Figures 4C, S22, and S23. In addition, the CVs recorded with the MAP = +1.5 V also reveal reproducible values (\pm 50 mV) of the first reduction potential $E^{(i1)}$, which remain unaltered during subsequent sweeps as observed in Figures 4D, S24, and S25. Congruent with these observations, the MAP-dependent CVs of PBI-(OC₂Triazo)-C₂Am-Si@2 interface shown in Figures 5B, S31, and S32 highlight the fact that resetting the MAP from +1.5 to +0.5 V has virtually no impact on the $E^{(i1)}$ value. Our findings underscore that PBI hybrid interfaces derived from molecularly dissolved building blocks do not enable a redox-assisted stabilization effect on conduction band energy.

Potentiometric Properties of Si Interfaces Featuring a Low Surface Density of PBIs. Because the redox-assisted

stabilization effect is witnessed exclusively for PBI- $(OC_2Triazo)$ - C_2Am -Si@1 interface constructed using π aggregated PBI units, we conclude that the solvated PBI aggregate precursors command the structure-function relationships of the PBI monolayers anchored covalently at the Si interface. To validate this hypothesis, PBI- (OC_2Az) - $C_2Am \pi$ aggregates were functionalized on Si electrodes that feature a low coverage of reactive alkyne moieties $(8.4 \times 10^{-12} \text{ mol})$ cm⁻²), 36,37 namely Si-(1:50)-Oct. Section 5B of the Supporting Information describes the synthetic details of the PBI-(OC₂Triazo)-C₂Am-Si(1:50)@1 interface. The solidstate morphology interrogated via tapping mode AFM image and the chemical composition monitored by high-resolution XPS spectra for these interfaces are summarized in Figures S11 and S14, respectively. Because the precursor alkyne-terminated surface Si-(1:50)-Oct features a population of one alkyne moiety per \sim 20 nm² surface area, 36,37 we posit that lateral π interactions between the PBI units is prohibited in PBI-(OC₂Triazo)-C₂Am-Si(1:50)@1 interface. In essence, the low density of reactive alkyne functions enables the anchorage of only a few PBI units featured in the solvated aggregates. Consequently, the PBI coverage in PBI-(OC₂Triazo)-C₂Am-Si(1:50)@1 is expected to contrast the PBI-(OC₂Triazo)-C2Am-Si@1 interface, which is characterized with a surface coverage of 2.23×10^{-10} mol cm⁻² for the PBI units translating to one PBI unit per 0.74 nm² surface area (please refer to Section 8.4 of the Supporting Information for details). In complete agreement with the surface coverage, the pertinent CVs recorded for the PBI-(OC, Triazo)-C, Am-Si(1:50)@1 interface (Figures S26 and S28) underscores divergently different potentiometric properties as compared to those evidenced for PBI-(OC₂Triazo)-C₂Am-Si@1 interface, vide supra. As shown in Figure S26, the sweep toward a cathodic potential (cycle 1) engenders a nonreversible potentiometric wave corresponding to an $E^{(i1)}_{\text{Cycle 1}}$ of -1.28 V. Sweeping back to the MAP of +0.5 V does not reveal any distinguishable redox signals. Surprisingly, the $E^{(i1)}$ undergoes an apparent cathodic shift during the sweep in cycle 2 $(E^{(i1)}_{Cycle\ 2} = -1.40$ V), which is restored during cycle 3. Setting the MAP to +1.5 V (Figure S28) reveals an $E^{(i1)}_{\text{Cycle 2}} = -1.44$ V, which resembles the $E^{(i1)}_{\text{Cycle 2}}$ evidenced while using MAP = +0.5 V. These potentiometric data vindicate that the PBI-(OC₂Triazo)-C₂Am-Si(1:50)@1 interface built from a low surface coverage of PBI units cannot initiate the redox-assisted stabilization effect observed exclusively for the PBI-(OC₂Triazo)-C₂Am-Si@1 interface that features a high density of anchoring precursors.

Origin of the Redox-Assisted Stabilization Effect. The origin of the redox-assisted stabilization effect on the conduction band energy of PBI-(OC₂Triazo)-C₂Am-Si@1 interface is anticipated to stem from the formation of nascent electronic trap states created within the π -aggregated PBI monolayer at MAP = +1.5 V. We posit that such developing electronic trap states are generated via structural deformations of π -aggregated PBI monolayer at a high anodic potential.³⁷ We have recently shown by DFT calculations that the p-doping of a model PBI trimer π -stack is associated with nonnegligible conformational perturbation.³⁷ Molecularly dissolved bay-functionalized PBI building blocks are known to undergo anodic oxidation in the solution state within the potential range of ca. +1.20 to +1.60 V vs SCE depending on the substituents.^{42,69,70} The oxidation potential of PBI units anchored covalently at the PBI-(OC₂Triazo)-C₂Am-Si@1

interface is expected to diverge, to some extent, in comparison with those witnessed in the solvated environment due to lateral interactions between the π -conjugated cores. The use of MAP = +1.5 V during the anodic sweep can facilitate injection of positive charge carriers (holes) into the valence bands of π -aggregated PBI units in PBI-(OC₂Triazo)-C₂Am-Si@1 interface. This claim is corroborated by the apparition of an anodic wave peaking at +1.28 V, as shown in Figures 4B, 5A, S20, and S29, during the anodic sweep to MAP = +1.5 V during cycle 1. This anodic peak may be attributed to p-doping (hole injection) of the π -aggregated PBI monolayer. This is further verified by the absence of this anodic peak during sweeping to MAP = +1.5 V in the case of PBI-(OC₂Triazo)-C₂Am-Si@2 interface engineered from molecularly dissolved PBI units as chronicled in Figures 4D, 5B, S24, and S31.

The redox-assisted stabilization effect presented herein mimics that we recently reported for hybrid interfaces built with π -aggregates derived from the terminally substituted PBI units shown in Scheme 1B.³⁷ However, the magnitude of the stabilization effect evidenced by the PBI-(OC2Triazo)-C2Am-Si@1 interface (295 mV) is lower (~80 mV) than that reported with interfaces constructed with PBI units not functionalized at the bay positions (375 mV).37 This observation validates that the precursor PBI π -aggregates can be exploited to modulate the final semiconducting properties of hybrid Si interfaces. The structure-function relationships of the π -aggregates derived from bay-substituted neutral PBI building block PBI-(OC₂Az)-C₂Am differ, to some extent, from those characterizing the terminally substituted neutral PBI building block PBI-C₂Am-C₂Az (Scheme 1B) recently reported by us.³⁷ This conclusion is corroborated by GS-EAS, solid-state morphology elucidated by SEM, and potentiometric properties recorded for the solvated π -aggregates of PBI- (OC_2Az) - C_2Am and PBI- C_2Am - C_2Az in MeOH/H₂O (50:1, v/v). For example, while PBI-C₂Am-C₂Az π -aggregates form fiber-like structures in the solid-state,³⁷ PBI-(OC₂Az)-C₂Am π -aggregates cannot evolve into hierarchical structures in the solid state. In addition, the spectroscopic signatures, and the potentiometric properties of the two π -aggregates in solution are drastically different, further suggesting that they exhibit different superstructure conformations. Accordingly, we conclude that the monolayers engineered from the precursor π-aggregates of PBI-(OC₂Az)-C₂Am (bay-substituted) and PBI-C₂Am-C₂Az (terminally substituted)³⁷ capture the structure—function relationships of the precursor π -aggregates. In essence, the conformations of the π -aggregate precursors are translated at the monolayer level, consequently parameterizing the magnitude of structural reconfiguration induced via pdoping at MAP = +1.5 V. Furthermore, we cannot rule out that some structural reorganization of the solvated aggregates occurs during the Si electrode functionalization step. Structural constraints imposed at Si interfaces may engender the formation of aggregated PBI monolayers whose conformation diverges as compared to that of the solvated PBI precursor assemblies. We posit that transferring the structure-function relationships of PBI π -aggregates on Si electrodes offers a powerful strategy to develop electroresponsive hybrid materials with redox-tunable conduction band energies.

CONCLUSIONS

We have shown that the aggregation state of a novel baysubstituted PBI building block can be harnessed to implement reversible electronic functionalities in semiconducting hybrid interfaces. Precisely, anchoring PBI π -aggregates on Si electrodes delivers the semiconducting monolayer PBI- $(OC_2Triazo)$ - C_2Am -Si@1, whose conduction band energies are dynamically regulated via a redox-assisted stabilization effect. While a MAP = +0.5 V instigates a cathodic reduction signal at -0.455 V, increasing the MAP to +1.5 V initiates a stabilization of 295 mV of the first cathodic reduction potential $(E^{(i1)}_{Cycle2} = -0.160$ V). We further demonstrate that this effect is reversible by switching between the two alternate MAP limits. Contrasting this result, the hybrid interface PBI- $(OC_2Triazo)$ - C_2Am -Si@2 derived from molecularly dissolved PBI units reveals that the conduction band energy is insensitive to the MAP applied during the oxidation cycles.

These findings are rationalized based on the formation of electronic trap states formed within the π -aggregated PBI monolayer through conformational perturbations. Emergent electronic trap states formed seemingly stabilize the conduction band energy of the interface. These emergent states facilitate the injection of negative charge carriers at more anodic potentials. To further demonstrate that the reported redox-assisted stabilization effect originates from lateral interaction between the PBI units, precursor Si interface featuring a low density of anchoring moieties was used to construct the PBI-(OC₂Triazo)-C₂Am-Si(1:50)@1 monolayer. In this interface, one reactive site is present every 20 nm² consequently preventing any lateral interactions between PBI units. Despite using PBI π -aggregates as a precursor, the PBI-(OC₂Triazo)-C₂Am-Si(1:50)@1 monolayer does not exhibit the redox-assisted stabilization effect reported for interfaces where lateral interaction between PBI modules is possible. This finding confirms the pivotal role of PBI π aggregates in tuning the conduction band energies of n-type monolayers functionalized at semiconducting Si hybrid interfaces. Furthermore, the hybrid Si interfaces derived from bay-functionalized PBIs show a stabilization effect whose magnitude is lower than that previously reported for monolayers built with terminally substituted PBIs.³⁷ This observation confirms that the structure-function relationships of the PBI π -aggregates are essential parameters to consider to modulate the semiconducting properties of n-type PBI-Si nanointerfaces.

By validating the fact that the semiconducting properties of hybrid Si interfaces can be reversibly tuned through the structure—function relationships of π -aggregates, the present study offers new opportunities to engineer electroresponsive functional monolayers for applications in the cutting-edge research areas of energy transduction, potentiometric memory devices, and information storage.

ASSOCIATED CONTENT

Supporting Information

The Supporting Information is available free of charge at https://pubs.acs.org/doi/10.1021/acs.langmuir.1c03423.

Synthetic details, sample preparation, SEM and AFM images, cyclic voltammograms, XPS spectra, NMR spectra, IR spectra, MS spectra (PDF)

AUTHOR INFORMATION

Corresponding Author

Jean-Hubert Olivier – Department of Chemistry, University of Miami, Cox Science Center, Coral Gables, Florida 33146,

United States; orcid.org/0000-0003-0978-4107; Phone: +1 305 284 3279; Email: jh.olivier@miami.edu

Authors

Arindam Mukhopadhyay — Department of Chemistry, University of Miami, Cox Science Center, Coral Gables, Florida 33146, United States; orcid.org/0000-0002-0620-4157

Kaixuan Liu – Department of Chemistry, University of Miami, Cox Science Center, Coral Gables, Florida 33146, United States

Victor Paulino – Department of Chemistry, University of Miami, Cox Science Center, Coral Gables, Florida 33146, United States; orcid.org/0000-0001-8916-3604

Complete contact information is available at: https://pubs.acs.org/10.1021/acs.langmuir.1c03423

Author Contributions

The manuscript was written through the contributions of all authors. All authors have given approval to the final version of the manuscript.

Notes

The authors declare no competing financial interest.

ACKNOWLEDGMENTS

We are grateful to the Arnold and Mabel Beckman Foundation (BYI 2018 Award) for the generous funding to support our research projects on the functionalization of hybrid Si interfaces. We are also thankful to the National Science Foundation (CAREER Award CHE-1941410) for supporting our research projects on redox-assisted assembly of π -conjugated chromophores. We are grateful to Dr. Carrie Donley who collected the XPS data at the Chapel Hill Analytical and Nanofabrication Laboratory (CHANL), a member of the North Carolina Research Triangle Nanotechnology Network (RTNN), which is supported by the National Science Foundation (Grant CCS-1542015) as part of the National Nanotechnology Coordinated Infrastructure (NNCI).

REFERENCES

- (1) Brédas, J.-L.; Norton, J. E.; Cornil, J.; Coropceanu, V. Molecular Understanding of Organic Solar Cells: The Challenges. *Acc. Chem. Res.* **2009**, *42*, 1691–1699.
- (2) Facchetti, A. π -Conjugated Polymers for Organic Electronics and Photovoltaic Cell Applications. *Chem. Mater.* **2011**, *23*, 733–758.
- (3) Armao, J. J., IV; Maaloum, M.; Ellis, T.; Fuks, G.; Rawiso, M.; Moulin, E.; Giuseppone, N. Healable Supramolecular Polymers as Organic Metals. *J. Am. Chem. Soc.* **2014**, *136*, 11382–11388.
- (4) Olivier, J. H.; Park, J.; Deria, P.; Rawson, J.; Bai, Y.; Kumbhar, A. S.; Therien, M. J. Unambiguous Diagnosis of Photoinduced Charge Carrier Signatures in a Stoichiometrically Controlled Semiconducting Polymer-Wrapped Carbon Nanotube Assembly. *Angew. Chem., Int. Ed.* 2015, 127, 8251–8256.
- (5) Stoltzfus, D. M.; Donaghey, J. E.; Armin, A.; Shaw, P. E.; Burn, P. L.; Meredith, P. Charge Generation Pathways in Organic Solar Cells: Assessing the Contribution from the Electron Acceptor. *Chem. Rev.* **2016**, *116*, 12920–12955.
- (6) Bai, Y.; Olivier, J.-H.; Yoo, H.; Polizzi, N. F.; Park, J.; Rawson, J.; Therien, M. J. Molecular Road Map to Tuning Ground State Absorption and Excited State Dynamics of Long-Wavelength Absorbers. *J. Am. Chem. Soc.* **2017**, *139*, 16946–16958.
- (7) Bloom, B. P.; Liu, R.; Zhang, P.; Ghosh, S.; Naaman, R.; Beratan, D. N.; Waldeck, D. H. Directing Charge Transfer in Quantum Dot Assemblies. *Acc. Chem. Res.* **2018**, *51*, 2565–2573.

- (8) Kulkarni, C.; Mondal, A. K.; Das, T. K.; Grinbom, G.; Tassinari, F.; Mabesoone, M. F.; Meijer, E.; Naaman, R. Highly Efficient and Tunable Filtering of Electrons' Spin by Supramolecular Chirality of Nanofiber-Based Materials. *Adv. Mater.* 2020, 32, No. 1904965.
- (9) Lorenzo, E. R.; Olshansky, J. H.; Abia, D. S.; Krzyaniak, M. D.; Young, R. M.; Wasielewski, M. R. Interaction of Photogenerated Spin Qubit Pairs with a Third Electron Spin in DNA Hairpins. *J. Am. Chem. Soc.* **2021**, *143*, 4625–4632.
- (10) Madhu, M.; Ramakrishnan, R.; Vijay, V.; Hariharan, M. Free Charge Carriers in Homo-Sorted π -Stacks of Donor–Acceptor Conjugates. *Chem. Rev.* **2021**, *121*, 8234–8284.
- (11) Buriak, J. M. Organometallic Chemistry on Silicon and Germanium Surfaces. *Chem. Rev.* **2002**, *102*, 1271–1308.
- (12) Love, J. C.; Estroff, L. A.; Kriebel, J. K.; Nuzzo, R. G.; Whitesides, G. M. Self-Assembled Monolayers of Thiolates on Metals as a Form of Nanotechnology. *Chem. Rev.* **2005**, *105*, 1103–1170.
- (13) Onclin, S.; Ravoo, B. J.; Reinhoudt, D. N. Engineering Silicon Oxide Surfaces Using Self-Assembled Monolayers. *Angew. Chem., Int. Ed.* **2005**, *44*, 6282–6304.
- (14) Fabre, B. Ferrocene-Terminated Monolayers Covalently Bound to Hydrogen-Terminated Silicon Surfaces. Toward the Development of Charge Storage and Communication Devices. *Acc. Chem. Res.* **2010**, 43, 1509–1518.
- (15) Ciampi, S.; Harper, J. B.; Gooding, J. J. Wet Chemical Routes to the Assembly of Organic Monolayers on Silicon Surfaces via the Formation of Si–C Bonds: Surface Preparation, Passivation and Functionalization. *Chem. Soc. Rev.* **2010**, 39, 2158–2183.
- (16) Gooding, J. J.; Ciampi, S. The Molecular Level Modification of Surfaces: From Self-Assembled Monolayers to Complex Molecular Assemblies. *Chem. Soc. Rev.* **2011**, *40*, 2704–2718.
- (17) Tian, F.; Teplyakov, A. V. Silicon Surface Functionalization Targeting Si–N Linkages. *Langmuir* **2013**, *29*, 13–28.
- (18) Fabre, B. Functionalization of Oxide-Free Silicon Surfaces with Redox-Active Assemblies. *Chem. Rev.* **2016**, *116*, 4808–4849.
- (19) Kherbouche, I.; Luo, Y.; Félidj, N.; Mangeney, C. Plasmon-Mediated Surface Functionalization: New Horizons for the Control of Surface Chemistry on the Nanoscale. *Chem. Mater.* **2020**, 32, 5442–5454
- (20) Park, J.; Belding, L.; Yuan, L.; Mousavi, M. P.; Root, S. E.; Yoon, H. J.; Whitesides, G. M. Rectification in Molecular Tunneling Junctions Based on Alkanethiolates with Bipyridine—Metal Complexes. J. Am. Chem. Soc. 2021, 143, 2156—2163.
- (21) Dionne, E. R.; Toader, V.; Badia, A. Microcantilevers Bend to the Pressure of Clustered Redox Centers. *Langmuir* **2014**, *30*, 742–752.
- (22) Liu, F.; Luber, E. J.; Huck, L. A.; Olsen, B. C.; Buriak, J. M. Nanoscale Plasmonic Stamp Lithography on Silicon. *ACS Nano* **2015**, *9*, 2184–2193.
- (23) Wadsworth, B. L.; Beiler, A. M.; Khusnutdinova, D.; Jacob, S. I.; Moore, G. F. Electrocatalytic and Optical Properties of Cobaloxime Catalysts Immobilized at a Surface-Grafted Polymer Interface. *ACS Catal.* **2016**, *6*, 8048–8057.
- (24) Dionne, E. R.; Dip, C.; Toader, V.; Badia, A. Micromechanical Redox Actuation by Self-Assembled Monolayers of Ferrocenylalkanethiolates: Evens Push More Than Odds. *J. Am. Chem. Soc.* **2018**, 140, 10063–10066.
- (25) Wong, R. A.; Yokota, Y.; Wakisaka, M.; Inukai, J.; Kim, Y. Discerning the Redox-Dependent Electronic and Interfacial Structures in Electroactive Self-Assembled Monolayers. *J. Am. Chem. Soc.* **2018**, 140, 13672–13679.
- (26) Robidillo, C. J. T.; Veinot, J. G. Functional Bio-inorganic Hybrids from Silicon Quantum Dots and Biological Molecules. *ACS Appl. Mater. Interfaces* **2020**, *12*, 52251–52270.
- (27) Li, S.; Wang, Y.; Wang, Y.; Sanvito, S.; Hou, S. High-Performance Spin Filters Based on 1,2,4,5-Tetrahydroxybenzene Molecules Attached to Bulk Nickel Electrodes. *J. Phys. Chem. C* **2021**, *125*, 6945–6953.
- (28) Carroli, M.; Dixon, A. G.; Herder, M.; Pavlica, E.; Hecht, S.; Bratina, G.; Orgiu, E.; Samorì, P. Multiresponsive Nonvolatile

- Memories Based on Optically Switchable Ferroelectric Organic Field-Effect Transistors. *Adv. Mater.* **2021**, *33*, No. 2007965.
- (29) Gauthier, N.; Argouarch, G.; Paul, F.; Humphrey, M. G.; Toupet, L.; Ababou-Girard, S.; Sabbah, H.; Hapiot, P.; Fabre, B. Silicon Surface-Bound Redox-Active Conjugated Wires Derived From Mono- and Dinuclear Iron (II) and Ruthenium (II) Oligo (phenyleneethynylene) Complexes. *Adv. Mater.* **2008**, *20*, 1952–1956.
- (30) Ciampi, S.; Eggers, P. K.; Le Saux, G.; James, M.; Harper, J. B.; Gooding, J. J. Silicon (100) Electrodes Resistant to Oxidation in Aqueous Solutions: An Unexpected Benefit of Surface Acetylene Moieties. *Langmuir* **2009**, *25*, 2530–2539.
- (31) Ciampi, S.; James, M.; Le Saux, G.; Gaus, K.; Justin Gooding, J. Electrochemical "Switching" of Si (100) Modular Assemblies. *J. Am. Chem. Soc.* **2012**, *134*, 844–847.
- (32) Fabre, B.; Pujari, S. P.; Scheres, L.; Zuilhof, H. Micropatterned Ferrocenyl Monolayers Covalently Bound to Hydrogen-Terminated Silicon Surfaces: Effects of Pattern Size on the Cyclic Voltammetry and Capacitance Characteristics. *Langmuir* **2014**, *30*, 7235–7243.
- (33) Zhang, L.; Vogel, Y. B.; Noble, B. B.; Gonçales, V. R.; Darwish, N.; Brun, A. L.; Gooding, J. J.; Wallace, G. G.; Coote, M. L.; Ciampi, S. TEMPO Monolayers on Si(100) Electrodes: Electrostatic Effects by the Electrolyte and Semiconductor Space-Charge on the Electroactivity of a Persistent Radical. *J. Am. Chem. Soc.* **2016**, *138*, 9611–9619.
- (34) Goncales, V. R.; Lian, J.; Gautam, S.; Hagness, D.; Yang, Y.; Tilley, R. D.; Ciampi, S.; Gooding, J. J. Heterojunctions Based on Amorphous Silicon: A Versatile Surface Engineering Strategy To Tune Peak Position of Redox Monolayers on Photoelectrodes. *J. Phys. Chem. C* 2019, 124, 836–844.
- (35) Mukhopadhyay, A.; Bernard, B.; Liu, K.; Paulino, V.; Liu, C.; Donley, C.; Olivier, J.-H. Molecular Strategies to Modulate the Electrochemical Properties of P-Type Si (111) Surfaces Covalently Functionalized with Ferrocene and Naphthalene Diimide. *J. Phys. Chem. B* **2019**, *123*, 11026–11041.
- (36) Mukhopadhyay, A.; Paulino, V.; Liu, K.; Donley, C. L.; Bernard, B.; Shomar, A.; Liu, C.; Olivier, J.-H. Leveraging the Assembly of a Rylene Dye to Tune the Semiconducting Properties of Functionalized n-Type, Hybrid Si Interfaces. *ACS Appl. Mater. Interfaces* **2021**, *13*, 4665–4675.
- (37) Mukhopadhyay, A.; Liu, K.; Paulino, V.; Donley, C. L.; Olivier, J.-H. Silicon Electrodes Functionalized with Perylene Bisimide π -Aggregates for Redox-Controlled Stabilization of Semiconducting Nanointerfaces. *ACS Appl. Nano Mater.* **2021**, *4*, 8813–8822.
- (38) Hauquier, F.; Ghilane, J.; Fabre, B.; Hapiot, P. Conducting Ferrocene Monolayers on Nonconducting Surfaces. *J. Am. Chem. Soc.* **2008**, *130*, 2748–2749.
- (39) Charbonnaz, P.; Zhao, Y.; Turdean, R.; Lascano, S.; Sakai, N.; Matile, S. Surface Architectures Built around Perylenediimide Stacks. *Chem. Eur. J.* **2014**, *20*, 17143–17151.
- (40) Zheng, Y.; Giordano, A. J.; Shallcross, R. C.; Fleming, S. R.; Barlow, S.; Armstrong, N. R.; Marder, S. R.; Saavedra, S. S. Surface Modification of Indium—Tin Oxide with Functionalized Perylene Diimides: Characterization of Orientation, Electron-Transfer Kinetics and Electronic Structure. *J. Phys. Chem. C* **2016**, *120*, 20040—20048.
- (41) Yin, X.; Wang, Q.; Zheng, Y. J.; Song, Z.; bin Hassan, M. H.; Qi, D.; Wu, J.; Rusydi, A.; Wee, A. T. Molecular Alignment and Electronic Structure of N, N'-Dibutyl-3, 4, 9, 10-Perylene-Tetracarboxylic-Diimide Molecules on MoS2 Surfaces. ACS Appl. Mater. Interfaces 2017, 9, 5566–5573.
- (42) Shan, B.; Nayak, A.; Brennaman, M. K.; Liu, M.; Marquard, S. L.; Eberhart, M. S.; Meyer, T. J. Controlling Vertical and Lateral Electron Migration Using a Bifunctional Chromophore Assembly in Dye-Sensitized Photoelectrosynthesis Cells. J. Am. Chem. Soc. 2018, 140, 6493–6500.
- (43) Smith, C. E.; Xie, Z.; Bâldea, I.; Frisbie, C. D. Work Function and Temperature Dependence of Electron Tunneling through an N-Type Perylene Diimide Molecular Junction with Isocyanide Surface Linkers. *Nanoscale* **2018**, *10*, 964–975.

- (44) Carl, A. D.; Grimm, R. L. Covalent Attachment and Characterization of Perylene Monolayers on Si (111) and TiO2 for Electron-Selective Carrier Transport. *Langmuir* **2019**, *35*, 9352–9363.
- (45) Zheng, Y.; Giordano, A. J.; Marder, S. R.; Saavedra, S. S. Potential-Modulated Total Internal Reflection Fluorescence for Measurement of the Electron Transfer Kinetics of Submonolayers on Optically Transparent Electrodes. *Langmuir* 2020, 36, 6728–6735.
- (46) Würthner, F. Perylene Bisimide Dyes as Versatile Building Blocks for Functional Supramolecular Architectures. *Chem. Commun.* **2004**, 1564–1579.
- (47) Huang, C.; Barlow, S.; Marder, S. R. Perylene-3,4,9,10-tetracarboxylic Acid Diimides: Synthesis, Physical Properties, and Use in Organic Electronics. *J. Org. Chem.* **2011**, *76*, 2386–2407.
- (48) Würthner, F.; Saha-Möller, C. R.; Fimmel, B.; Ogi, S.; Leowanawat, P.; Schmidt, D. Perylene Bisimide Dye Assemblies as Archetype Functional Supramolecular Materials. *Chem. Rev.* **2016**, *116*, 962–1052.
- (49) Nowak-Król, A.; Würthner, F. Progress in the Synthesis of Perylene Bisimide Dyes. Org. Chem. Front. 2019, 6, 1272–1318.
- (50) Liang, N.; Meng, D.; Wang, Z. Giant Rylene Imide-Based Electron Acceptors for Organic Photovoltaics. *Acc. Chem. Res.* **2021**, 54, 961–975.
- (51) Leira-Iglesias, J.; Sorrenti, A.; Sato, A.; Dunne, P. A.; Hermans, T. M. Supramolecular Pathway Selection of Perylenediimides Mediated by Chemical Fuels. *Chem. Commun.* **2016**, *52*, 9009–9012.
- (52) Leira-Iglesias, J.; Tassoni, A.; Adachi, T.; Stich, M.; Hermans, T. M. Oscillations, Travelling Fronts and Patterns in a Supramolecular System. *Nat. Nanotechnol.* **2018**, *13*, 1021–1027.
- (53) Liu, K.; Levy, A.; Liu, C.; Olivier, J.-H. Tuning Structure–Function Properties of π -Conjugated Superstructures by Redox-Assisted Self-Assembly. *Chem. Mater.* **2018**, *30*, 2143–2150.
- (54) Liu, K.; Mukhopadhyay, A.; Ashcraft, A.; Liu, C.; Levy, A.; Blackwelder, P.; Olivier, J.-H. Reconfiguration of π -Conjugated Superstructures Enabled by Redox-Assisted Assembly. *Chem. Commun.* **2019**, 55, 5603–5606.
- (55) Krieg, E.; Niazov-Elkan, A.; Cohen, E.; Tsarfati, Y.; Rybtchinski, B. Noncovalent Aqua Materials Based on Perylene Diimides. *Acc. Chem. Res.* **2019**, *52*, 2634–2646.
- (56) Ashcraft, A.; Liu, K.; Mukhopadhyay, A.; Paulino, V.; Liu, C.; Bernard, B.; Husainy, D.; Phan, T.; Olivier, J. H. A Molecular Strategy to Lock-in the Conformation of a Perylene Bisimide-Derived Supramolecular Polymer. *Angew. Chem., Int. Ed.* **2020**, *59*, 7487–7493.
- (57) Liu, K.; Paulino, V.; Mukhopadhyay, A.; Bernard, B.; Kumbhar, A.; Liu, C.; Olivier, J.-H. How to Reprogram the Excitonic Properties and Solid-State Morphologies of π-Conjugated Supramolecular Polymers. *Phys. Chem. Chem. Phys.* **2021**, 23, 2703–2714.
- (58) Hestand, N. J.; Spano, F. C. Molecular Aggregate Photophysics Beyond the Kasha Model: Novel Design Principles for Organic Materials. *Acc. Chem. Res.* **2017**, *50*, 341–350.
- (59) Hestand, N. J.; Spano, F. C. Expanded Theory of H- and J-Molecular Aggregates: The Effects of Vibronic Coupling and Intermolecular Charge Transfer. *Chem. Rev.* **2018**, *118*, 7069–7163.
- (60) Chen, Z.; Baumeister, U.; Tschierske, C.; Würthner, F. Effect of Core Twisting on Self-Assembly and Optical Properties of Perylene Bisimide Dyes in Solution and Columnar Liquid Crystalline Phases. *Chem. Eur. J.* **2007**, *13*, 450–465.
- (61) Elgrishi, N.; Rountree, K. J.; McCarthy, B. D.; Rountree, E. S.; Eisenhart, T. T.; Dempsey, J. L. A Practical Beginner's Guide to Cyclic Voltammetry. *J. Chem. Educ.* **2018**, *95*, 197–206.
- (62) Shirman, E.; Ustinov, A.; Ben-Shitrit, N.; Weissman, H.; Iron, M. A.; Cohen, R.; Rybtchinski, B. Stable Aromatic Dianion in Water. *J. Phys. Chem. B* **2008**, *112*, 8855–8858.
- (63) Schlosser, F.; Moos, M.; Lambert, C.; Würthner, F. Redox-switchable Intramolecular π - π -Stacking of Perylene Bisimide Dyes in a Cyclophane. *Adv. Mater.* **2013**, *25*, 410–414.
- (64) Higashi, T.; Sagara, T. Diphenyl Viologen on an HOPG Electrode Surface: Less Sharp Redox Wave than Dibenzyl Viologen. *Langmuir* **2013**, 29, 11516–11524.

- (65) Avestro, A. J.; Gardner, D. M.; Vermeulen, N. A.; Wilson, E. A.; Schneebeli, S. T.; Whalley, A. C.; Belowich, M. E.; Carmieli, R.; Wasielewski, M. R.; Stoddart, J. F. Gated Electron Sharing within Dynamic Naphthalene Diimide-Based Oligorotaxanes. *Angew. Chem., Int. Ed.* **2014**, *53*, 4442–4449.
- (66) Paulino, V.; Mukhopadhyay, A.; Tsironi, I.; Liu, K.; Husainy, D.; Liu, C.; Meier, K.; Olivier, J.-H. Molecular Engineering of Water-Soluble Oligomers to Elucidate Radical π -Anion Interactions in n-Doped Nanoscale Objects. *J. Phys. Chem. C* **2021**, *125*, 10526–10538.
- (67) Espinoza, E. M.; Clark, J. A.; Soliman, J.; Derr, J. B.; Morales, M.; Vullev, V. I. Practical Aspects of Cyclic Voltammetry: How to Estimate Reduction Potentials When Irreversibility Prevails. *J. Electrochem. Soc.* **2019**, *166*, H3175.
- (68) Fabre, B.; Bassani, D. M.; Liang, C.-K.; Ray, D.; Hui, F.; Hapiot, P. Anthracene and Anthracene: C60 Adduct-Terminated Monolayers Covalently Bound to Hydrogen-Terminated Silicon Surfaces. *J. Phys. Chem. C* **2011**, *115*, 14786–14796.
- (69) Vajiravelu, S.; Ramunas, L.; Vidas, G. J.; Valentas, G.; Vygintas, J.; Valiyaveettil, S. Effect of Substituents on the Electron Transport Properties of Bay Substituted Perylene Diimide Derivatives. *J. Mater. Chem.* **2009**, *19*, 4268–4275.
- (70) Zhang, F.; Ma, Y.; Chi, Y.; Yu, H.; Li, Y.; Jiang, T.; Wei, X.; Shi, J. Self-assembly, Optical and Electrical Properties of Perylene Diimide Dyes Bearing Unsymmetrical Substituents at Bay Position. *Sci. Rep.* **2018**, *8*, 1–11.

□ Recommended by ACS

Thermal Insolubilization of Electrically n-Doped Films Achieved Using 7-Alkoxy-Benzocyclobutene-Substituted Fullerene and Dopant Molecules

Farzaneh Saeedifard, Stephen Barlow, et al.

SEPTEMBER 28, 2022

THE JOURNAL OF PHYSICAL CHEMISTRY B

RFAD 🗹

Revealing the Role of Polaron Distribution on the Performance of n-Type Organic Electrochemical Transistors

Junwei Shi, Ting Lei, et al.

JANUARY 06, 2022

CHEMISTRY OF MATERIALS

READ 🗹

Silicon Electrodes Functionalized with Perylene Bisimide π -Aggregates for Redox-Controlled Stabilization of Semiconducting Nanointerfaces

Arindam Mukhopadhyay, Jean-Hubert Olivier, et al.

AUGUST 23, 2021

ACS APPLIED NANO MATERIALS

READ **C**

Characteristic Control of n-Channel Organic Thin-Film Transistors Using a Dimethyl-Substituted Benzimidazole Dopant

Kei Noda, Akihiro Ito, et al.

DECEMBER 03, 2021

ACS APPLIED ELECTRONIC MATERIALS

READ 🗹

Get More Suggestions >